

# Mesenchymal Stromal Cell-Mediated Treatment of Local and Systemic Inflammation through the Triggering of an Anti-Inflammatory Response

Jonathan O. Martinez,\* Michael Evangelopoulos, Ava A. Brozovich, Guillermo Bauza, Roberto Molinaro, Claudia Corbo, Xuewu Liu, Francesca Taraballi,\* and Ennio Tasciotti

The emergence of cell-based therapeutics, specifically the use of mesenchymal stromal/stem cells (MSCs), stands to significantly affect the future of targeted drug delivery technologies. MSCs represent a unique cell type, offering more than only regenerative potential but also site-specific inflammatory targeting and tissue infiltration. In this study, a versatile multicomponent delivery platform, combining MSC tropism with multistage nanovector (MSV)-mediated payload delivery, is debuted. It is demonstrated that the incorporation of drug-loaded MSVs bestows MSCs with the ability to transport anti-inflammatory payloads, achieving a fivefold increase in payload release without negatively impacting cellular functions, viability, extravasation, and inflammatory homing. When incorporated within MSCs, MSVs avoid rapid sequestration by filtering organs and conserve a 15-fold increase in local inflammatory targeting compared to healthy ears. Furthermore, this MSC-mediated MSV platform (M&Ms) rapidly triggers a 4.5-fold reduction of local inflammation compared to free drug and extends survival to 100% of treated mice in a lethal model of systemic inflammation.


“drugstores,” enabling medicinal MSCs for patient-specific therapy.<sup>[2]</sup> For what pertains therapeutic delivery applications, MSCs are innately advantageous compared to conventional pharmaceutical agents (i.e., small molecules, biologics). MSCs are capable of sensing, responding, making complex decisions, modulating immune activation, and directing migration to sites of inflammation.<sup>[3,4]</sup> However, despite promising preclinical findings, translating this potential to success in the clinic has proven to be elusive with variable results, possibly due to the short-term secretion of bioactive molecules after administration<sup>[5,6]</sup> or issues pertaining to their survival or clearance following infusion.<sup>[7]</sup> Hence, the triggering of MSCs to sustain the release of bioactive molecules is a to enhance their clinical efficacy and impact the more than 1425 clinical trials (as of August 2020, <http://clinicaltrials.gov>) currently using MSCs.<sup>[1]</sup>

## 1. Introduction

Traditional views of mesenchymal stromal/stem cells (MSCs) have focused on their multipotent differentiation ability. However, their anti-inflammatory, trophic, and immunomodulatory capabilities<sup>[1]</sup> have prompted their use as possible site-regulated

Nanoparticles offer tunable solutions to sustain the release of various molecules in a spatially and temporally controlled fashion, but their therapeutic efficacy has been hindered by their inadequate negotiation of biological barriers.<sup>[8]</sup> Multistage nanovectors (MSVs) were developed to negotiate and overcome the biological barriers faced during systemic

Dr. J. O. Martinez, M. Evangelopoulos, A. A. Brozovich, Dr. G. Bauza, Dr. R. Molinaro, Dr. C. Corbo, Dr. F. Taraballi, Dr. E. Tasciotti  
Center for Musculoskeletal Regeneration  
Houston Methodist Research Institute  
6670 Bertner Ave Houston, Houston, TX 77030, USA  
E-mail: jomartinez@houstonmethodist.org,  
jonathan.otto.martinez@gmail.com; ftaraballi2@houstonmethodist.org  
A. A. Brozovich, Dr. E. Tasciotti  
Texas A&M College of Medicine  
8447 Bryan Rd, Bryan, Houston, TX 77807, USA

 The ORCID identification number(s) for the author(s) of this article can be found under <https://doi.org/10.1002/adfm.202002997>.

© 2020 The Authors. Published by Wiley-VCH GmbH. This is an open access article under the terms of the Creative Commons Attribution-NonCommercial-NoDerivs License, which permits use and distribution in any medium, provided the original work is properly cited, the use is non-commercial and no modifications or adaptations are made.

A. A. Brozovich, Dr. F. Taraballi, Dr. E. Tasciotti  
Orthopedics and Sports Medicine  
Houston Methodist Hospital  
6565 Fannin Street Houston, Houston, TX 77030, USA

Dr. G. Bauza  
Center for NanoHealth  
Swansea University Medical School  
Swansea University Bay, Singleton Park  
Swansea, Wales SA2 8PP, UK

Dr. C. Corbo  
School of Medicine and Surgery  
Nanomedicine Center NANOMIB  
University of Milano-Bicocca  
Veduggio al Lambro, MB 20854, Italy

Dr. X. Liu  
Department of Nanomedicine  
Houston Methodist Research Institute  
Houston, TX 77030, USA

DOI: 10.1002/adfm.202002997

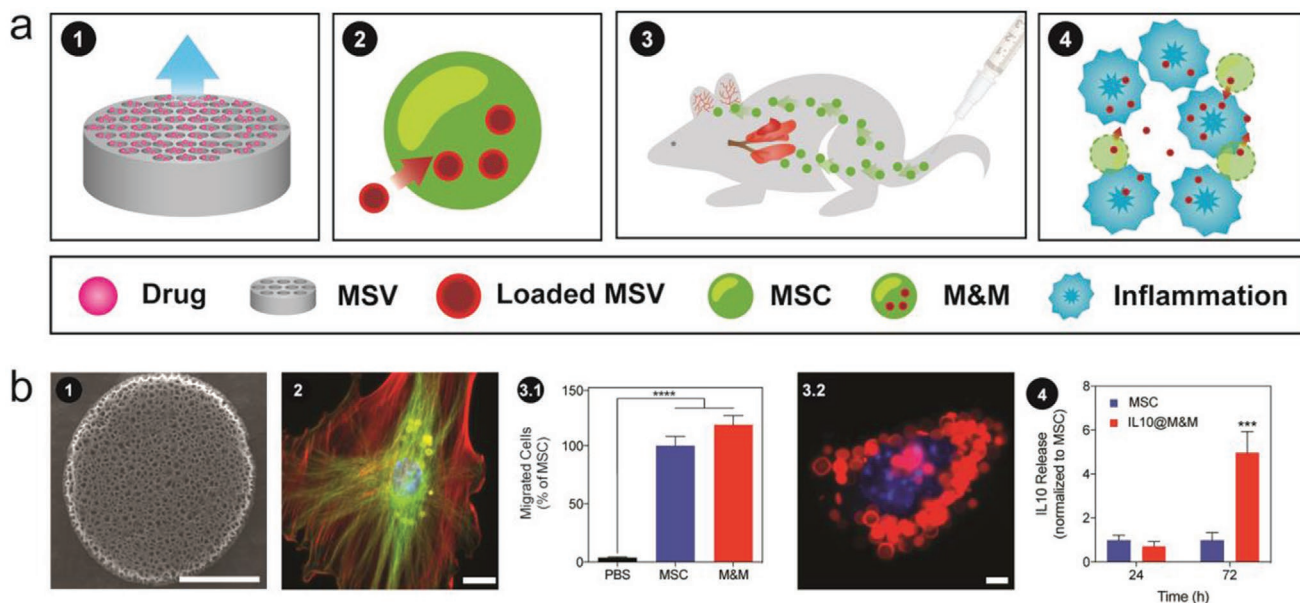


**Figure 1.** Assembly of M&M-based delivery platform. a) Schematic illustrating how MSVs and MSCs are combined to form the M&M delivery platform: 1) MSV loaded with desired payloads (i.e., drugs or nanoparticles) are 2) subsequently internalized and retained within MSCs 3) enabling homing to inflamed environments and 4) subsequent release of therapeutics at inflammatory site. b) Representative images corresponding to the steps described above: 1) SEM micrograph depicting the stage one MSV platform, scale bar: 1  $\mu\text{m}$ ; 2) fluorescence image showing the cytoskeleton features of MSCs containing internalized MSVs, scale bar: 20  $\mu\text{m}$ ; 3.1) quantification of migration of M&Ms and MSCs toward inflamed stimuli compared to MSCs affinity to a PBS control. 3.2) Fluorescence image illustrating the successful homing of MSCs, while carrying several MSVs to inflammatory stimuli, scale bar: 5  $\mu\text{m}$ ; 4) release of IL10 comparing MSCs and IL10@M&Ms. For all graphs: \* $p < 0.05$ , \*\*\* $p < 0.001$ , and \*\*\*\* $p < 0.0001$ , and values represent the mean with error bars as s.e.m.

administration.<sup>[8–11]</sup> Specifically, MSVs were designed to encompass multiple stages and allocate tasks onto these stages with the first stage (i.e., nanoporous microparticles) responsible for binding to diseased vasculature while protecting the cargo from degradation; subsequent stages (e.g., nanoparticles, therapeutics), therefore, are tasked with cellular targeting, promoting intracellular uptake, and therapy.<sup>[11]</sup> MSVs are fabricated utilizing biocompatible<sup>[12]</sup> and biodegradable nanoporous silicon<sup>[13]</sup> and have shown a remarkable capacity to load, retain, protect, and deliver payloads for imaging and therapy.<sup>[14,15]</sup> Additionally, MSV's versatile design has been used to prolong circulation by mimicking platelet<sup>[16]</sup> geometrical properties while convenient surface chemistry properties have been exploited to achieve active targeting.<sup>[17–20]</sup> Nevertheless, free MSVs have been hindered by rapid sequestration by filtering organs<sup>[19]</sup> thus minimizing their therapeutic potential. In addition, finding methods to delay this physiologic clearance and increase the targeting efficiency of MSVs to inflamed tissues remains an unexplored challenge.

Nanoparticles that have been attached to the surface (e.g., adsorbed, attached covalently or through ligand–receptor interactions as cellular backpacks) or internalized by cells represent a possible method to circumvent these barriers and chaperone a payload to the target site.<sup>[21–25]</sup> However, surface attachment of nanoparticles may damage cell membranes, trigger an immune response, obstruct cell–cell interactions, or cause detachment of nanoparticles during transportation due to shear stress or cell reshaping.<sup>[21]</sup> Similarly, while internalization (i.e., “Trojan Horse”) protects nanoparticles from interacting with filtering organs, it is affected by the cell's exocytotic processes and can

result in premature cell death if payloads are prematurely released.<sup>[26,27]</sup> One possible solution to address exocytosis of nanoparticles is the use of microparticles (i.e.,  $>1 \mu\text{m}$  in diameter) that allows for the retention of internalized nanoparticles or drugs, permitting cells to function naturally.

Lymphocytes, red blood cells, and monocytes/macrophages have previously been used to transport nanoparticles. However, MSCs represent an optimal cell source as they can home and transmigrate at sites of inflammation while readily internalizing nanoparticles, unlike red blood cells and lymphocytes.<sup>[21]</sup> In addition, MSCs can be easily isolated from multiple types of tissues (e.g., adipose, bone marrow, umbilical cord blood, etc.<sup>[28]</sup>), whereas monocytes are predominately isolated from the blood and bone marrow and are hindered by limited ex vivo life spans.<sup>[29]</sup> MSCs can also differentiate into cells of the mesodermal lineage whereas monocytes can only differentiate into macrophages and dendritic cells,<sup>[28]</sup> which enable additional unique features for tissue regeneration and inflammatory response. Additionally, MSCs have shown immunosuppression and low immunogenicity features, which have led to clinical studies for their ability to reduce immune response after implantation.<sup>[30]</sup>

Given these considerations, we developed a proof-of-concept approach (Figure 1a) to create an MSC–MSV platform (M&Ms) that combines MSCs with MSVs (Figure 1b-1), whose larger size (3  $\mu\text{m}$ ) minimizes the risk of exocytosis.<sup>[26]</sup> Furthermore, the physical size of MSVs provides a higher degree of control to deliver a precise number of particles to each cell, thus enabling a possible method to manage the dose received per cell (Figure S1, Supporting Information). Previous investigations

indicated that the internalization or exposure to MSVs showed no potent inflammatory response in vitro with macrophages<sup>[31]</sup> or in vivo in tumor-bearing mice<sup>[32]</sup> and did not affect the osteogenic or adipogenic differentiation of MSCs.<sup>[12]</sup> In this study, we leveraged the advantageous pharmacological features of MSVs with the unique inflammatory targeting features of MSCs by combining them via internalization. Our results indicate that by effectively merging nanotechnology and stem cell biology, it is possible to develop new applications that could improve the therapeutic outcome of MSC administration.

## 2. Results

### 2.1. MSCs with Internalized MSVs Permit Tuning of Dose per Cell, Migration, and Payload Release

Mouse bone marrow MSCs containing several internalized MSVs exhibited minimal impact on shape, cytoskeletal organization, and proliferation (Figure 1b-2; Figure S2, Supporting Information). Quantification of the number of MSVs internalized at various ratios revealed the ability to tune MSCs to obtain defined quanta to regulate the dose received by each cell (Figure S1, Supporting Information). In addition, MSCs conserved their ability to migrate in response to inflammatory signals, even when carrying a large MSV payload (Figure 1b-3). To assess the nanotriggering of MSCs using MSVs, we demonstrated that M&Ms loaded with a potent anti-inflammatory cytokine IL10<sup>[33]</sup> (IL10@M&M) exhibited sustained IL10 release at 72 h, providing a 4.97-fold increase in unstimulated MSC IL10 secretion (Figure 1b-4). Furthermore, the internalization of empty MSVs (M&Ms) did not cause a significant increase in the secretion of IL10 from MSCs confirming the impact of using IL10@M&Ms to induce release of payloads (Figure S3, Supporting Information). We anticipate that this drug release from M&Ms follows a similar pattern compared to previous publications where the therapeutic is passively released from MSVs, diffuses into the cytoplasm, and is transported across the cell membrane permitting it to interact with the surrounding environment.<sup>[34]</sup>

### 2.2. Impact of MSV Internalization of Transendothelial Migration of MSCs

The ability of MSCs to perform transendothelial migration<sup>[35,36]</sup> (dock, adhere, crawl, and transmigrate; **Figure 2a**) is critical for the therapeutic success of M&Ms. We tested whether M&Ms could specifically dock and stably adhere to inflamed endothelia using an in vitro reconstructed syngeneic vascular environment. After inflammatory activation of primary mouse pulmonary vein endothelial cells (MPVECs), both M&Ms and MSCs significantly docked to inflamed endothelia (Figure 2b,c) and remained persistently attached, even in the presence of physiological shear stress, while displaying only minimal adhesion to noninflamed MPVECs (Figures S4 and S5, Supporting Information). To mimic the physiological shear stresses experienced during venular (0.1–4.0 dyn cm<sup>-2</sup>) and arterial ( $\geq 5$  dyn cm<sup>-2</sup>)<sup>[37]</sup> blood flow, we measured the adhesion strength of MSCs at

fixed and varying shear stresses (0.1–10 dyn cm<sup>-2</sup>). At fixed shear stresses of 0.1 and 1.0 dyn cm<sup>-2</sup>, M&Ms and MSCs exhibited a similar decrease in adhesion of 90% to 45%, respectively, with a significant increase observed at 0.5 dyn cm<sup>-2</sup> for M&Ms (Figure 2d). Gradual increases in shear stresses, up to arterial shear forces, led to stable adhesion with similar dynamics for both MSC groups, with greater than 75% of cells adhering at 10 dyn cm<sup>-2</sup> (Figure 2e; Movies S1 and S2, Supporting Information), suggesting M&Ms were capable of adhering under relevant shear forces. Analysis of time-lapse microscopy (Movie S3, Supporting Information) revealed that during flow-induced crawling both groups exhibited similar morphological changes under flow and executed intravascular-like crawling with comparable crawling velocities (0.04 and 0.13  $\mu\text{m s}^{-1}$ ), and covering similar distances (5 and 16  $\mu\text{m}$ ) at 0.1 and 1.0 dyn cm<sup>-2</sup>, respectively (Figure 2f–h; Figure S6 and S7, Supporting Information). After adhesion, both groups successfully induced interendothelial cell gaps within the monolayer (Movie S4, Supporting Information), suggesting effective paracellular diapedesis.<sup>[35]</sup> By modeling the inflamed vascular barrier using a Transwell system (Figure 2i), we observed that M&Ms conserved their ability to undergo diapedesis, displaying cell protrusions through the Transwell pores (Figure 2j), indicating that MSVs have no impact on overall MSC transmigration (Figure 2k).

### 2.3. M&Ms Delay Physiologic Clearance and Increase Targeting Efficiency of MSVs to Inflamed Tissues

To understand if the in vitro results translated in vivo, a syngeneic animal model capable of recapitulating the intrinsic features governing mouse MSC tropism (e.g., cellular pathways, signal transduction, and cell to cell communication) was used. We examined their sequestration by filtering organs (liver, spleen, kidney) and retention of their site-specific inflammatory homing. 1 h after systemic administration, MSVs persisted within MSCs (Figure S8, Supporting Information) and displayed significantly lower accumulation (approximately tenfold), compared to free MSVs, in liver, spleen, and kidney (**Figure 3a–c**). Lungs were the major accumulation site for both groups with a significant difference found for M&M organ accumulation ratios of lungs-to-liver and lungs-to-spleen (Figure S9, Supporting Information).

A local inflammatory site was established by direct ear injection of lipopolysaccharide (LPS), with the contralateral ear serving as control, to measure the ability of M&Ms to retain site-specific inflammatory homing. Inflammation was confirmed using longitudinal bioluminescence imaging (BLI) of luminol to monitor the expression of myeloperoxidase, an enzyme expressed by activated phagocytes.<sup>[38]</sup> Previous studies validated the use of BLI with luminol for inflammation assessment using histological analysis to confirm BLI correlated with infiltration of neutrophils/eosinophils.<sup>[38]</sup> BLI images showed that inflammation was confined to the right ear, with signal concentrating at the base of the ear and propagating away to the tip of the ear (Figure 3d). Quantification confirmed that both groups displayed significant differences between the two ears, confirming inflammation was predominately found in the right (i.e., inflamed) ear (Figure 3e). In the same mice, the

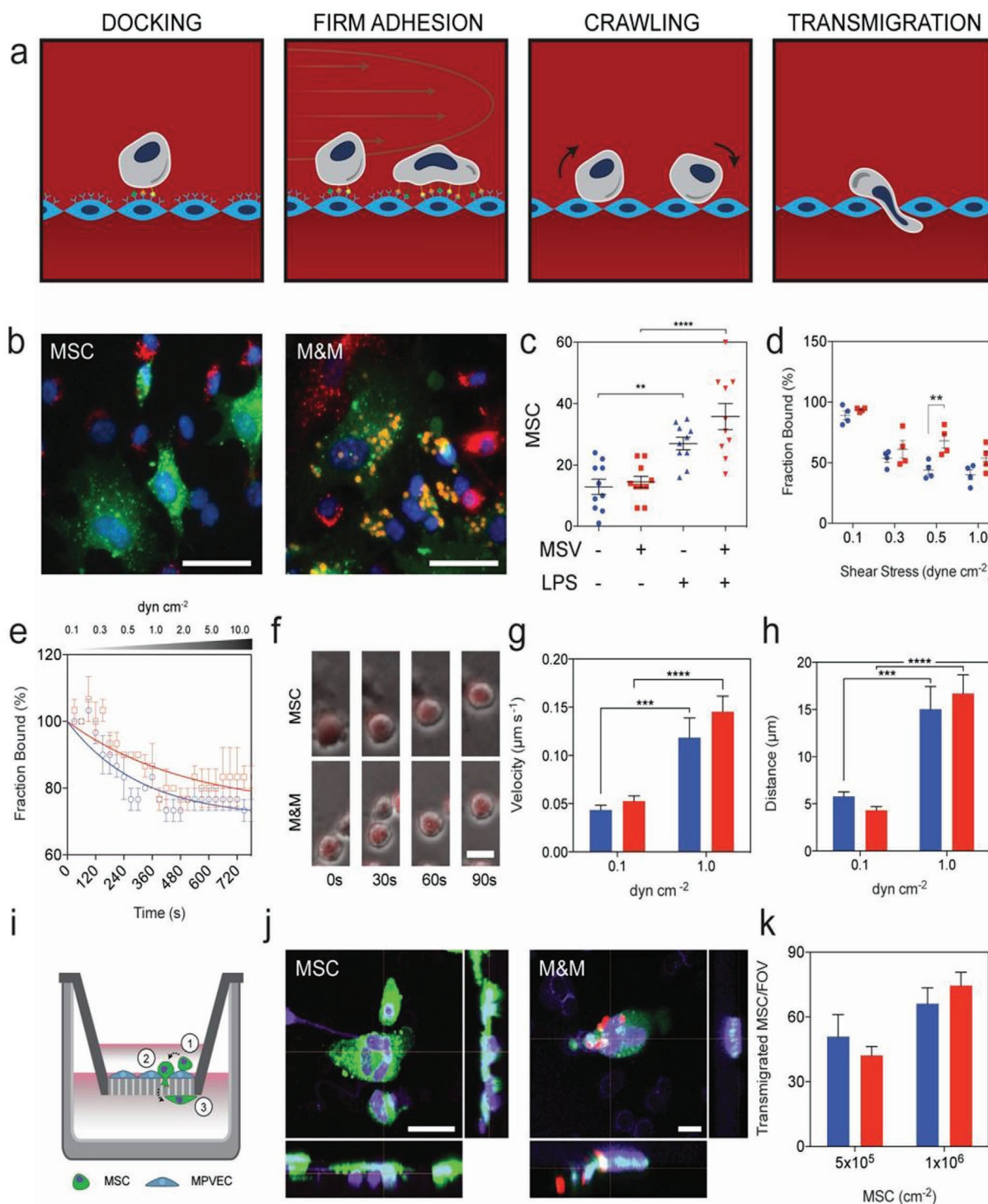


**Figure 2.** M&Ms in vitro negotiation of inflamed endothelia. a) Schematic displaying four crucial steps of the cell adhesion cascade to achieve efficient homing and targeting of inflammatory stimuli. b) MSCs (green) with DAPI-stained nuclei (blue) containing MSVs (orange) demonstrated conserved docking on inflamed MPVECs (red); scale bars: 50  $\mu\text{m}$ . c) Quantification of docking comparing the propensity of MSCs to discriminate between healthy and inflamed endothelia. Firm adhesion quantification of MSCs and M&Ms at d) fixed shear stresses and e) varying shear stresses. f) Representative images comparing the crawling of M&Ms and MSCs on inflamed endothelia, with MSCs shown in red; scale bars: 25  $\mu\text{m}$ . Quantification of the g) crawling velocity and h) distance crawled by M&Ms and MSCs. i) Schematic illustrating the arrangement of transwells used to study the transmigration of MSCs across an inflamed endothelial monolayer. j) Fluorescence images of MSCs (green) seeded on transwells and captured during the process of transmigration through the pores of the transwell, the nuclei (blue) of both cells (MSC and MPVEC) are shown; scale bar: 10  $\mu\text{m}$ . k) Quantification of the transmigration of M&Ms and MSCs at the two indicated concentrations of MSCs. For all graphs:  $**p < 0.01$ ,  $***p < 0.001$ , and  $****p < 0.0001$ , and values represent the mean with error bars as s.e.m.

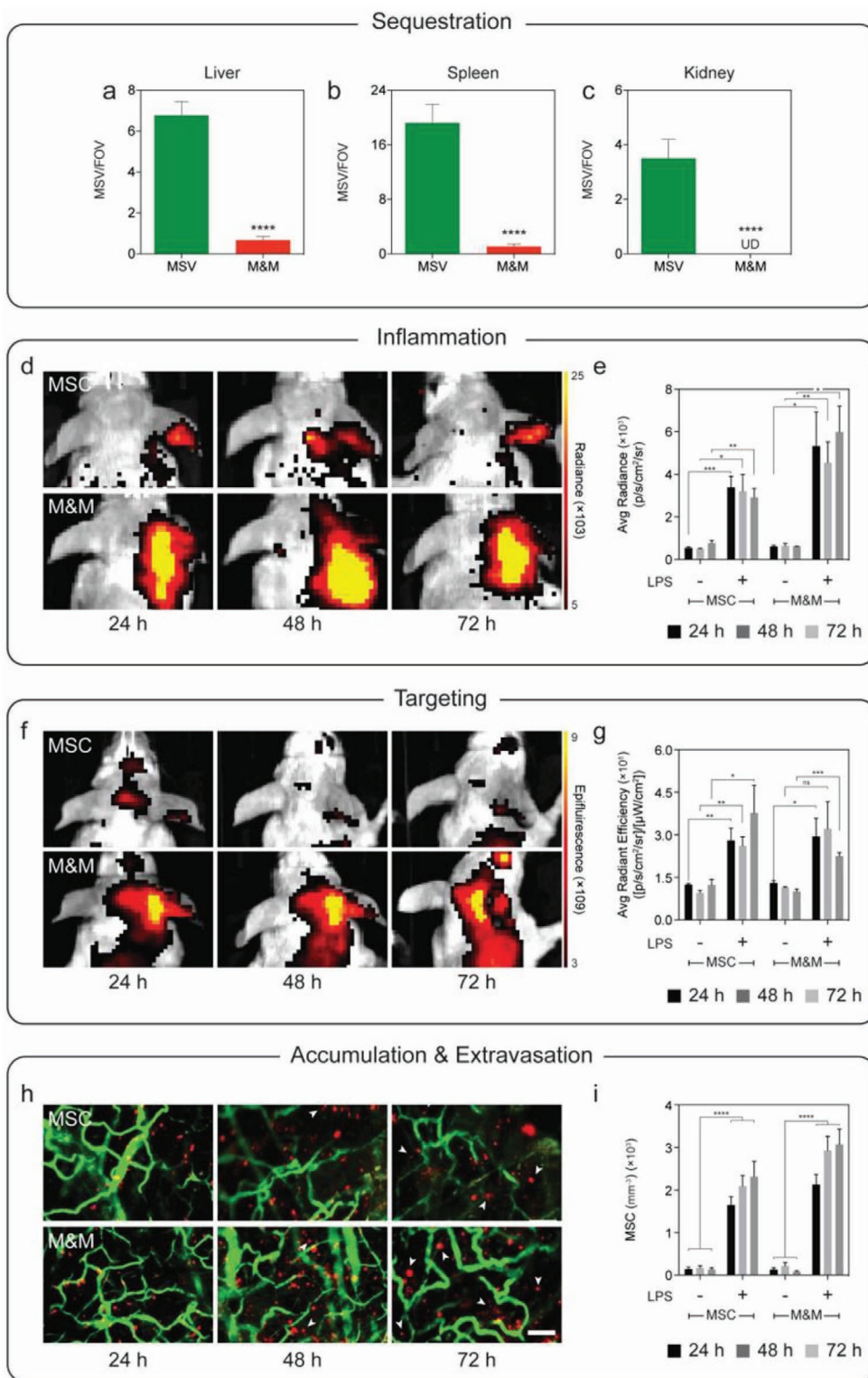


**Figure 3.** Evasion of phagocytic cell sequestration and directed inflammatory targeting. Quantification of MSVs counted per field-of-view (FOV) in the a) liver, b) spleen, and c) kidney observed 1 h after systemic administration in healthy mice. d) Representative BLI images and e) quantification to assess the extent of inflammation in the ears of mice (left ear = healthy and right ear = inflamed) at 24, 48, and 72 h. f) Representative images of DiD fluorescence and g) quantification to evaluate the homing of M&Ms and MSCs toward sites of local inflammation at 24, 48, and 72 h. h) Representative IVM images and i) quantification of M&Ms and MSCs homing to inflamed ears at 24, 48, and 72 h. Within the images in (h), the vasculature is delineated in green (FITC dextran) and MSC in red (DiD) showing increased numbers of transmigrated cells (white arrows); scale bars: 100  $\mu\text{m}$ . For all graphs: \* $p < 0.05$ , \*\* $p < 0.01$ , \*\*\* $p < 0.001$ , and \*\*\*\* $p < 0.0001$ , and values represent the mean with error bars as s.e.m.

distribution of DiD-labeled MSCs were simultaneously imaged with whole-animal fluorescent imaging and confirmed that both M&Ms and MSCs homed selectively to inflamed ears (Figure 3f). Quantification validated these observations showing significant accumulation of MSCs in inflamed ears ranging from 2.5- to 3-fold increased targeting compared to control ears (Figure 3g). Also, signals in inflamed ears remained constant from 24 to 72 h with negligible differences between MSCs and M&Ms.

Corroboration of whole-animal imaging of MSC accumulation in ears was verified using intravital microscopy (IVM). Images from IVM provided a detailed analysis of the cellular dynamics in the ear confirming preferential targeting to inflamed ears (Figure 3h; Figure S10a, Supporting Information). Additional inspection at 48 and 72 h revealed M&Ms conserved the migratory dynamics of MSCs, displaying increased and similar extravasation over time (Figure 3h, white arrows). Quantification analysis showed a 15-fold increase in preferential tropism of MSCs and M&Ms to inflamed ears, exhibiting similar kinetics observed in whole-animal analysis (Figure 3i). Administration of free MSVs resulted in minimal accumulation for normal and inflamed ears (Figure S10b, Supporting Information). Furthermore, to evaluate the impact of MSVs on the biodistribution of MSCs, we quantified the accumulation of MSCs and M&Ms by ex vivo analysis of organs 5 days after administration in the local inflammatory model (Figure S10c, Supporting Information). Comparative analysis revealed that no significant difference was found between MSCs and M&Ms within each organ. Additionally, both groups retained more than a threefold increase in targeting inflamed ears confirming the long-term targeting capacity. These results demonstrated that MSCs effectively modulated the biodistribution of MSVs, delayed their rapid sequestration and clearance, and mediated a 15-fold increase in inflammatory-targeting with minimal impact on the overall biodistribution of MSCs.

## 2.4. MSVs Empowered M&Ms to Alleviate Local Inflammation

To demonstrate the efficacy and therapeutic potential of M&Ms, we loaded IL10 and investigated their ability to reduce inflammation using the same local inflammatory model described above. BLI with luminol was used to assess the level of inflammation in the ears of mice within the first 24 h. Baseline inflammation in the ear was measured 3 h after LPS induction while treatment occurred at 6 h with response to therapy being measured at 9 and 24 h. Treatments ( $n = 5$ ) included untreated, free IL10 ( $1 \mu\text{g kg}^{-1}$ ), IL10@MSV ( $1 \mu\text{g kg}^{-1}$ ), MSCs, and IL10@M&Ms ( $1 \mu\text{g kg}^{-1}$ ). BLI images at 9 and 24 h show marked differences between IL10@M&Ms and all groups, displaying substantially less signal at 24 h (Figure 4a). Combined inflammatory quantification of raw values (Figure S11, Supporting Information) and normalization before therapy at 3 h (Figure 4b), confirmed that IL10@M&Ms exhibited significant decreases in inflammation at 9 and 24 h compared to untreated, free IL10, and IL10@MSV. Normalization to 3 h was carried out to account for the baseline variation in inflammation within the model that arises due to the small surface area available in the ear. Additional normalization accounting for the healthy (i.e., control) ear of

the same mouse, revealed that treatment with IL10@M&Ms significantly reduced inflammation at 24 h compared to all tested therapies (Figure 4c). Compared to free IL10, IL10@MSVs, and MSCs, IL10@M&Ms exhibited a 3-fold decrease in inflammation and a 4.5-fold decrease compared to untreated. In addition, higher doses of IL10 for free IL10 and IL10@MSVs did not yield any advantage in decreasing local inflammation at 24 h (Figure S12, Supporting Information). Hence, treatment with IL10@M&Ms at  $1 \mu\text{g kg}^{-1}$  exhibited a significant decrease in inflammation while using an >80% reduced dose.

Examination of excised treated mouse ears showed various degrees of redness and edema (Figure S13, Supporting Information). This change of appearance has been correlated with significant inflammatory cellular infiltrates in ears showing an abundance of granulocytes (i.e., neutrophils, eosinophils, etc.).<sup>[39]</sup> Inflamed ears collected from mice treated with IL10@M&Ms showed less edema compared to other treatments indicating treatment possibly reduced the accumulation of inflammatory cells in ears (Figure S13, Supporting Information). Hematoxylin and eosin (H&E) stained ear sections of mice from the various groups at 24 h confirmed this observation and the assessment from BLI of luminol (Figure 4d). Gross analysis of treated ears demonstrated a wide difference within the experimental groups. H&E images showed normal ear tissue architecture for healthy mice, whereas untreated, free IL10, and IL10@MSV exhibited substantial alteration of the ear's architecture with increased neutrophil infiltration and edema observed. Mice treated with MSCs appear to have a milder infiltration of inflammatory cells. The most potent anti-inflammatory response was observed for mice treated with IL10@M&Ms with ears revealing substantial reduced inflammation, edema, and infiltration of inflammatory cells compared to all other treatment groups.

## 2.5. MSVs Bestowed M&Ms to Enable Prolonged Survival in a Systemic Model of Inflammation

The ability of M&Ms to dampen systemic inflammation was assessed by loading dexamethasone (DEX), a synthetic glucocorticoid for the treatment of inflammation,<sup>[40]</sup> and evaluating the response in a LPS-induced sepsis-related mouse model.<sup>[41]</sup> Previous investigations using a septic model demonstrated that MSCs permitted 35% survival when given 1 h after induction, with 10% survival observed in untreated mice at 96 h.<sup>[42]</sup> In our experiments, treatment ( $n = 5$ ) with untreated, free DEX ( $1$  and  $5 \text{ mg kg}^{-1}$ ), DEX@MSV ( $1 \text{ mg kg}^{-1}$ ), MSCs, MSC+DEX ( $5 \text{ mg kg}^{-1}$ ), and DEX@M&Ms ( $1 \text{ mg kg}^{-1}$ ) began 30 min after challenging mice with LPS. Mice in untreated, free DEX at  $1$  and  $5 \text{ mg kg}^{-1}$ , and DEX@MSVs at  $1 \text{ mg kg}^{-1}$  groups demonstrated 100% death before 26 h (Figure 5a; Figure S14, Supporting Information). As free DEX at  $5 \text{ mg kg}^{-1}$  yielded slightly better survival results, we chose to use mice treated at  $5 \text{ mg kg}^{-1}$  for additional comparative analysis. Treatment with MSCs yielded survival in 20% of mice and matches well with previous results given that our model demonstrated higher lethality. However, combination therapy with MSCs and DEX (i.e., MSC+DEX) did not yield an increased survival benefit with no mouse surviving more than 24 h. On the other hand,

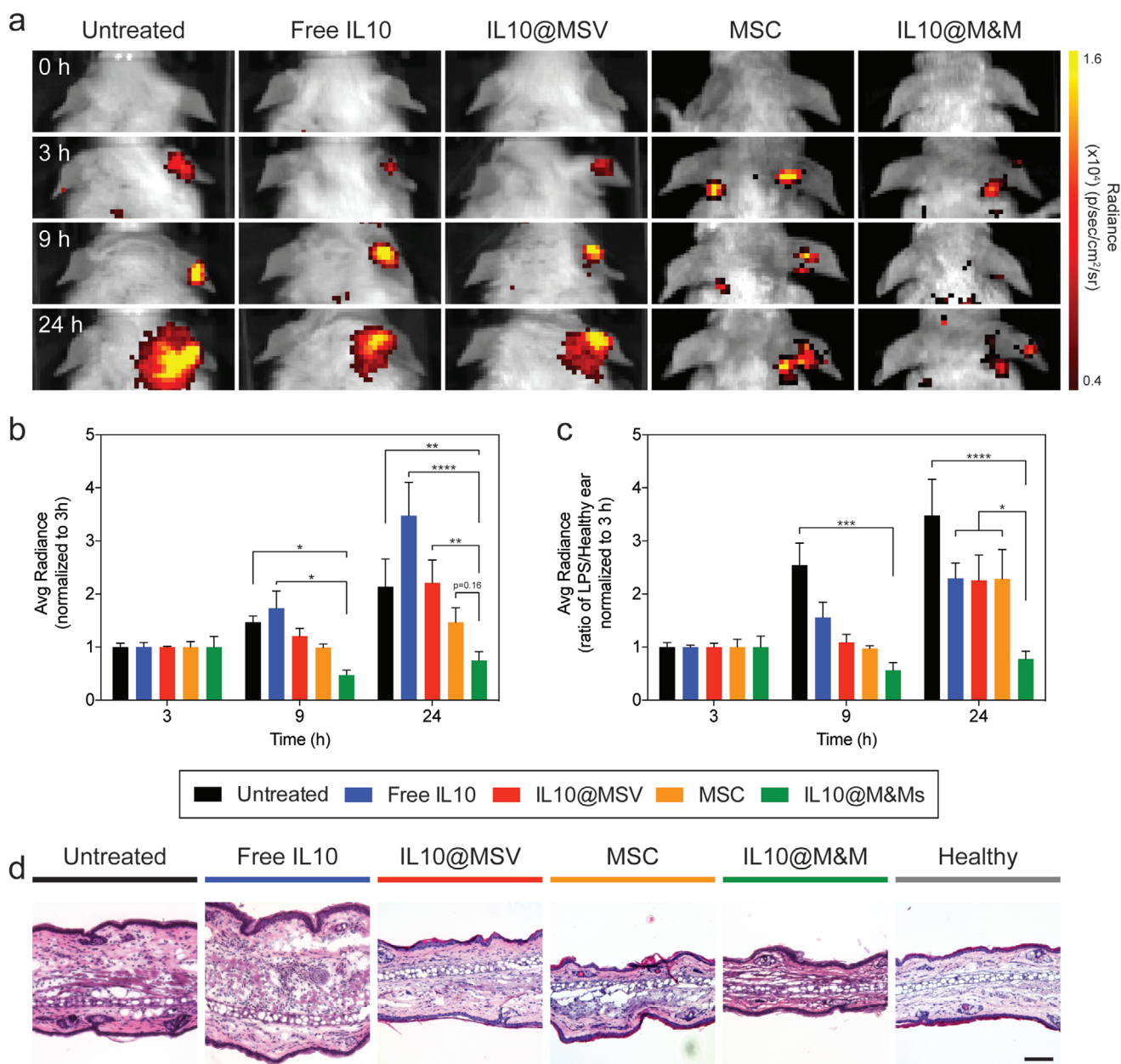


**Figure 4.** Nanotriggered MSC treatment alleviates local inflammation in mice. a) Representative BLI images displaying the extent of local inflammation in the ears of mice at 0, 3, 9, and 24 h post-LPS administration. Inflammation was assessed using luminol to image recruitment of activated phagocytes. b,c) Treatment effects on local inflammation as reflected by quantification of BLI signals at 0, 3, 9, and 24 h post-LPS administration. Data shown were adjusted to b) normalize to 3 h and c) account for healthy ear, revealing the impact of therapy by adjusting for the degree of LPS induction in each group and within each mouse, respectively. d) Sections of ears from mice of the indicated treatment group at 24 h stained with H&E; scale bar: 50  $\mu$ m. The sections show a substantial alteration of tissue architecture with massive edema and infiltration of immune cells in untreated, free IL10, and IL10@MSV ears. Milder responses were observed in mice treated with MSCs and IL10@M&Ms, with the most potent response seen in mice treated with IL10@M&Ms. For all graphs: \* $p < 0.05$ , \*\* $p < 0.01$ , \*\*\* $p < 0.001$ , and \*\*\*\* $p < 0.0001$ , and values represent the mean with error bars as s.e.m.

treatment with DEX@M&Ms, at 1 mg kg<sup>-1</sup> or an 80% reduced dose of DEX compared with free DEX, significantly increased survival with 100% survival observed at 120 h.

As this model induces a severe lung injury,<sup>[41]</sup> we examined levels of tumor necrosis factor-alpha (TNF- $\alpha$ ) (Figure 5b; Figure S15, Supporting Information) and lung histology (Figure 5c,d) at 18 and 120 h. Plasma TNF- $\alpha$  at 18 h of mice treated with free DEX and DEX@MSV displayed similar

plasma TNF- $\alpha$  levels to untreated, whereas mice treated with MSC displayed a  $\approx 25\%$  decrease (Figure 5b).

Interestingly, mice treated with MSC+DEX did not show a synergistic impact on plasma TNF- $\alpha$  which showed an  $\approx 20\%$  increase compared to untreated, confirming the lack of survival shown in Figure 5a. Conversely, plasma TNF- $\alpha$  levels in healthy (no LPS) mice and mice treated with DEX@M&Ms were undetectable (UD) and were all significantly lower compared to

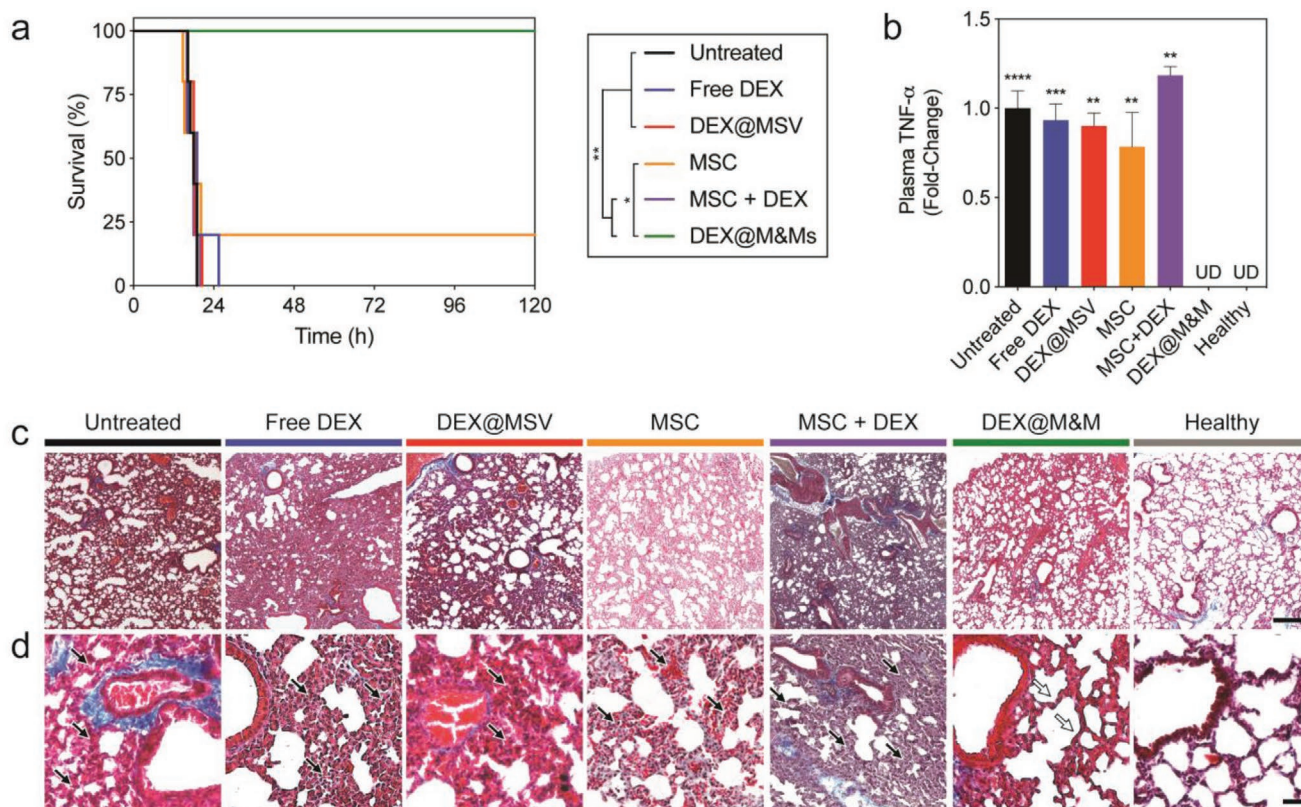


**Figure 5.** Nanotriggered M&Ms prolong survival of mice with systemic inflammation. a) Survival curves of mice after systemic inflammation activation by a lethal dose of LPS, monitoring mice up to 120 h. b) Quantification of TNF- $\alpha$  in the plasma of mice treated with the indicated treatments and compared to healthy mice, 18 h after inflammatory induction. c) Lung tissue sections at 18 h postinflammatory induction stained with Masson's Trichrome; scale bar: 200  $\mu\text{m}$ . d) Higher magnification images of lung section in (c) with black arrows indicating spots where there is substantial engorgement of capillary vessels, obliteration of alveolar spaces, and severe loss of alveolar structure; and white arrows (in DEX@M&Ms) indicating the moderately conserved alveoli structure; scale bar 50  $\mu\text{m}$ . For all graphs: \* $p < 0.05$ , \*\* $p < 0.01$ , and \*\*\* $p < 0.001$ , and values represent the mean with error bars as s.e.m.

other treatments. Inspection of pulmonary TNF- $\alpha$  revealed that mice treated with DEX@MSVs and DEX@M&Ms displayed significantly lower levels than untreated mice (Figure S15, Supporting Information). This organ-specific effect for DEX@MSV and DEX@M&M may be attributed to their ability to accumulate in the lungs at similar levels (Figure S9A,B, Supporting Information). Furthermore, the difference in the ability of DEX@M&Ms to demonstrate a systemic effect, compared to DEX@MSVs, could be attributed to the rapid sequestration of MSVs by MPS organs (Figure 3a–c), which hindered the ability of DEX@MSVs to deliver any DEX systemically. As M&Ms did not exhibit this behavior, it is possible they remained in or re-entered<sup>[43]</sup> circulation longer and enabled enhanced systemic delivery of DEX. Whereas DEX@MSVs and free DEX was unsuccessful, DEX@M&Ms suppressed both pulmonary and plasma TNF- $\alpha$  levels which may explain the survival advantage of this treatment group. In addition, at 120 h, pulmonary TNF- $\alpha$  levels from DEX@M&M-treated mice exhibited significantly lower levels compared to 18 h indicating an ongoing recovery (Figure S15, Supporting Information).

Furthermore, histological analysis of lung tissues recovered at 18 h showed considerable differences in lung architecture between DEX@M&Ms and other treatment groups (Figure 4c,d). Sections from untreated, free DEX, DEX@MSV,

MSCs, and MSC+DEX-treated mice uncovered considerable engorgement of capillary vessels, accumulation of nonspecific inflammatory cells, obliteration of alveolar spaces, and severe loss of alveolar structure (Figure 4d, black arrows). However, lungs at 18 h from DEX@M&M-treated mice displayed moderately conserved alveolar trabecular structure (Figure 4d, gray arrows) and did not exhibit any substantial accumulation of nonspecific inflammatory cells or swelling of capillary vessels. In addition, sections recovered after 120 h demonstrated an absence of a prolonged inflammatory response and signs of recovery (Figure S16, Supporting Information). All together, these in vivo results indicate that MSCs containing MSVs may serve as effective cellular vehicles for local and systemic anti-inflammatory therapy.

### 3. Discussion

The use of MSCs has been proven safe; however, conflicting accounts concerning their homing, mechanism of action, survival or clearance after administration, and inability to standardize therapy have hindered their clinical translation.<sup>[5,7]</sup> Nanotriggering of MSCs to enhance or induce specific



responses (e.g., targeted anti-inflammatory action) holds considerable promise for precision therapy.<sup>[1]</sup> Herein, we conceived a versatile, hybrid (half-cell/half-synthetic) delivery platform combining MSC tropism with MSV-regulated payload delivery, enabling various classes of nanotriggered MSCs with the option to deliver multiple payloads<sup>[10]</sup> in defined quanta to regulate the dose received by each cell. MSCs efficiently internalized large quantities of MSVs, permitting the transport and delivery of large payloads and achieve prolonged release of anti-inflammatory agents. Furthermore, M&Ms conserved MSC's function for successful inflammatory targeting by recognizing, docking, adhering, crawling, and transmigrating at the site of inflamed endothelia. Additionally, we demonstrated that M&Ms evaded phagocytic cell sequestration and transmigrated through inflamed vasculature, which represent two critical biological barriers hindering most nanoparticles.<sup>[8]</sup> Lastly, M&Ms enhanced MSC-mediated local and systemic anti-inflammatory effects, bestowing a survival advantage to treated animals. Thus, the MSV platform works synergistically with MSCs permitting the retention of innate stem cell features and targeting of inflammation without exacerbating the inflammatory process to support the use of M&M-based therapy to augment or enhance therapeutic action of MSCs.

In contrast to other cell-based systems, this proof-of-principle strategy achieved full therapeutic success (100% animal survival) by applying an easily standardizable approach to introduce unique features to cells, without requiring any extensive gene manipulation<sup>[44]</sup> or preconditioning with drugs.<sup>[45,46]</sup> Furthermore, the versatility of MSVs permits the incorporation and tailoring of a wide array of therapeutic or diagnostic payloads within MSCs, enabling refined anti-inflammatory theranostic regimens.<sup>[13,47,48]</sup> Chronic inflammation can lead to multiple pathologies, including atherosclerosis, cancer, and inflammatory bowel and pulmonary diseases.<sup>[49]</sup> Thus, development of specific targeting platforms to target, prevent, or resolve inflammation is greatly warranted.<sup>[50,51]</sup>

Current targeting strategies for nanoparticles (e.g., active and passive) require their transport to be at a precise location to be effective, however, their ability to target or interact with vessel walls is regulated by blood flow and often fail to actively counteract the biological barriers that impede their transport.<sup>[8]</sup> Modifications to avert this clearance (e.g., polyethylene glycol coatings) reduced uptake, decreased efficacy, and elevated immune responses, resulting in increased complexity in the synthesis with minimal therapeutic improvement.<sup>[52–54]</sup> A major obstacle within the transport of MSCs is the entrapment in lungs. However, unlike nanoparticles, the entrapment of MSCs in lungs could be temporary<sup>[43]</sup> as they can sense, respond, and actively migrate to the target, providing a direct and dynamic delivery of nanoparticles while minimizing immune response in part due to the innate tropism and immune evasion of MSCs.<sup>[3,55]</sup> Furthermore, in clinical studies with MSCs, minimal impact on lungs has been observed and studies for patients with lung cancer, chronic obstructive pulmonary disease, emphysema, acute respiratory distress syndrome, and idiopathic pulmonary fibrosis revealed that MSCs were considered safe.<sup>[56]</sup> Hence, leveraging on the physiology of the body has the potential to bring a paradigm shift in nanotechnology,<sup>[19,57]</sup> the hybrid nature of M&Ms embodies this theme and represents a promising

bioinspired delivery platform to nanotrigger the therapeutic potency of MSCs.

## 4. Experimental Section

**Source and Culture of MSCs:** MSCs were isolated from the bone marrow of several (three to five) healthy BALB/c and pooled together, as previously described,<sup>[58,59]</sup> and used for in vitro experiments; whereas primary mouse BALB/c bone marrow MSCs purchased from Cell Biologics were used in vivo. Briefly, for isolation, mice were sacrificed, and the femurs and tibia were harvested, stripped of muscle. Bone marrow was flushed and plated into a large petri dish with alpha MEM supplemented with 20% fetal bovine serum (FBS, Thermo Scientific) in a 37 °C in a 5% CO<sub>2</sub> and 5% O<sub>2</sub> atmosphere. Upon reaching confluency, cells were collected and characterized for the expression of primary mesenchymal-associated markers with a Fortessa cell analyzer (Beckton Dickinson), under the assistance of the HMRI Flow Cytometry Core. The cells were tested to be negative for the markers CD19 (BD Pharmingen), CD34 (BioLegend), and CD45 (BD Pharmingen). Positive tested markers included the endoglin (CD105, BioLegend), the ecto-5'-nucleotidase CD73 (BioLegend), and the glycoprotein CD44 (BioLegend). This characterization was performed for MSCs, IL10@M&Ms, and DEX@M&Ms to confirm that the cells' phenotype was not affected by the treatment.

**Assembly of M&M Delivery System:** The M&M delivery system consisted of 3-aminopropyltriethoxysilane (APTES)-modified 3 μm MSV that were passively loaded with free drug (IL-10 or DEX) and then internalized by MSCs. MSVs were fabricated using facilities at the Microelectronics Research Center at The University of Texas at Austin and the HMRI Nanoparticles Core, as previously described.<sup>[60]</sup> Prior to APTES, MSVs were oxidized by Piranha etch to create hydroxyl groups on the surface as previously described.<sup>[32]</sup> After oxidation, MSVs were modified with APTES (Sigma-Aldrich). Briefly, MSVs were resuspended in a solution containing 2% APTES and 5% water and incubated at 35 °C with mixing at 1300 rpm for 2 h. Samples were washed three times in IPA and stored in a vacuum desiccator overnight. IL10 (Peprotech) was loaded in APTES-modified MSV particles, through a loading procedure, previously optimized.<sup>[61]</sup> 10 μg of IL10 was reconstituted in 150 μL of PBS (Gibco) under sterile conditions. APTES-modified MSV, previously dried in a vacuum oven (Thermo Scientific) overnight, was dispersed in the IL10 solution, and mixed at 300 rpm in a thermomixer (Thermo Scientific) for 4 h at 37 °C. MSVs were then recovered and lyophilized. The loading efficiency of IL10 in MSVs was calculated by measuring the IL10 left in the loading solution, by IL10 Quantikine ELISA kit (R&D Systems). Similar to the loading of IL10, DEX (Sigma-Aldrich) was loaded into MSV. Briefly, APTES-modified MSV, previously dried in a vacuum oven (Thermo Scientific) overnight, was dispersed in a DEX solution, and mixed at 300 rpm in a thermomixer (Thermo Scientific) for 4 h at 37 °C. MSVs were recovered and dried. The loading efficiency of DEX in MSV was calculated by measuring the DEX left in the loading solution, by HPLC. MSVs were then exposed to MSCs seeded at near confluency to allow internalization overnight. Additional details about MSV fabrication, MSV surface modification, and internalization is provided in the Supporting Information.

**Migration to Inflammatory Stimuli:** The migration of M&Ms and MSCs was assessed using similar methods, as previously described.<sup>[12]</sup> Briefly, 4T1 cells were seeded onto 24-well plates at 20 000 cells per well and allowed to adhere overnight. The subsequent day, 8.0 μm transwells (Greiner Bio-One) were placed into wells and 2 × 10<sup>4</sup> MSC and M&M at 50:1 MSV:MSC ratio were seeded in the top chamber of the transwells in serum-free media. Wells containing PBS, rather than 4T1 cells, served as the negative control. Plates were incubated at 37 °C and 5% CO<sub>2</sub> for 24 h. MSC that successfully invaded the transwell were recovered as described earlier for transmigration experiments. Recovered cells were seeded into four-chamber glass slides (LabTek) for 2–3 h to allow for attachment. MSCs were fixed in 4% PFA and mounted with Prolong Gold containing

DAPI. Slides were imaged with a Nikon Eclipse 80i fluorescence microscope equipped with a monochromatic Andor DL-604M camera and counting the MSCs using Nikon Elements software. Measurements represented biological triplicates with samples from 12 random fields-of-view (FOVs).

**Prolonged Release of IL10:** MSCs were left untreated or treated with MSVs (empty or IL10@MSVs). MSCs were allowed to incubate with MSVs overnight to ensure internalization. The following day, MSCs were harvested and seeded in triplicates in 24-well plates. At predetermined times, the media from the wells was collected (i.e., extracellular IL10) and analyzed using the aforementioned ELISA kit. Measurements represented biological triplicates with a technical replicate.

**Docking, Firm Adhesion, and Transmigration—Activation/Docking:** MPVECs and MSCs were labeled with DiO and DiD (Invitrogen), respectively. Cells were stained with these lipophilic dyes at  $1 \times 10^6$  cells  $\text{mL}^{-1}$  in phosphate-buffered saline (PBS) containing the respected dye at  $10 \times 10^{-6}$  M at room temperature for 20 min followed by washes in PBS. For static assessment,  $7 \times 10^4$  MPVECs were seeded into four-chambered glass slides (LabTek) and allowed to adhere overnight. The following day, MPVECs were either treated with complete media (noninflamed or control) or complete media containing 50 ng  $\text{mL}^{-1}$  of murine TNF- $\alpha$  (eBioscience) (i.e., inflamed or activated) for 18 h.  $2 \times 10^4$  MSCs (+/- MSV at 1:25 ratio labeled with Alexa Fluor 555) were added to MPVECs and were allowed to adhere for 60 min at 37 °C and 5%  $\text{CO}_2$ , and then were carefully washed with PBS, fixed with 4% PFA for 10 min, and mounted with Prolong Gold containing DAPI (Invitrogen). For dynamic assessment, MPVECs were seeded into ibidi  $\mu$ -Slide<sup>10.4</sup> Leur ibiTreated slides (ibidi GmbH) and were coated with human fibronectin at 75  $\mu\text{g}$   $\text{mL}^{-1}$  at a density of  $1.5 \times 10^6$  cells  $\text{mL}^{-1}$  and were allowed to adhere overnight before treatment with complete media or 50 ng  $\text{mL}^{-1}$  of TNF- $\alpha$  in complete media for 18 h. DiD-labeled MSCs (+/- MSV labeled with Alexa Fluor 555) were seeded at  $1 \times 10^6$  cells  $\text{mL}^{-1}$  and allowed to adhere on inflamed/noninflamed MPVECs for 20 min. Slides were exposed to 0.5 dyn  $\text{cm}^{-2}$  and imaged continuously for 60 min. Images from each chamber or  $\mu$ -slide were acquired using inverted Nikon Eclipse Ti fluorescence microscope equipped with a Hamamatsu ORCA-Flash 2.8 digital camera and fitted with an induction chamber maintaining samples at 37 °C and 5%  $\text{CO}_2$ . MSCs in each image were counted using Nikon Elements. Measurements represented samples from ten random FOV technical replicates per sample and condition.

**Docking, Firm Adhesion, and Transmigration—Firm Adhesion and Crawling:** MPVECs were seeded on ibidi  $\mu$ -slide<sup>10.4</sup> Leur precoated with human fibronectin at 75  $\mu\text{g}$   $\text{mL}^{-1}$  at a density of  $1.5 \times 10^6$  cells  $\text{mL}^{-1}$  and were allowed to adhere overnight before treatment with 50 ng  $\text{mL}^{-1}$  of TNF- $\alpha$  in complete media. For fixed shear, individual  $\mu$ -slides were treated with MSCs or M&Ms. MSCs were allowed to adhere to MPVECs for 3 min seeding at  $0.5 \times 10^6$  cells  $\text{mL}^{-1}$ . Slides were exposed to 0.1, 0.3, 0.5, or 1.0 dyn  $\text{cm}^{-2}$  and were continuously imaged, as described earlier, for 5 min. Each slide was analyzed for the number of MSCs present before and after the addition of flow. For varying shear, MSCs and M&Ms were equally mixed together to create a solution of  $1 \times 10^6$  cells  $\text{mL}^{-1}$  and seeded onto the same  $\mu$ -slide containing inflamed MPVECs and allowed to adhere for 5 min. The shear stress exposed to cells began at 0.1 dyn  $\text{cm}^{-2}$  and was increased after 120 s to 0.3 dyn  $\text{cm}^{-2}$ . This increase in shear stress continued for the remainder of the experiment increasing to 0.5, 1.0, 2.0, 5.0, and 10.0 dyn  $\text{cm}^{-2}$  (10.0 was exposed only for 30 s). Cells were monitored continuously for 750 s as described earlier. Measurements represented at least three random FOV technical replicates for each sample and shear stress. To examine crawling, images from the fixed shear experiments at 0.1 and 1.0 dyn  $\text{cm}^{-2}$  were analyzed for MSC dynamics. Crawling velocities, distance moved, and polar graphs were calculated using Nikon Elements software equipped with object tracking. Measurements represented samples from the movement of at least 35 technical replicates of MSCs.

**Docking, Firm Adhesion, and Transmigration—Transmigration:** To evaluate the early steps of paracellular transmigration of MSCs, MPVECs were seeded onto ibidi  $\mu$ -slides as described in the previous section and allowed to adhere overnight. Following overnight incubation, cells

were inflamed with 50 ng  $\text{mL}^{-1}$  of TNF- $\alpha$  in complete media. Real-time paracellular transmigration was monitored by treating  $\mu$ -slides with DiO-labeled MSCs (+/- MSV labeled with Alexa Fluor 555) at  $6 \times 10^5$  cell  $\text{mL}^{-1}$ . MSCs were allowed to adhere for 15 min before being exposed to 0.5 dyn  $\text{cm}^{-2}$  for 1 h. Images were acquired every 3 min and visualized for pore formation within the monolayer. To assess transmigration across an inflamed endothelium,  $9 \times 10^4$  MPVECs were seeded onto 8  $\mu\text{m}$  transwells (Greiner Bio-One) in 24-well plates and allowed to adhere overnight. The following day, MPVECs were activated with 50 ng  $\text{mL}^{-1}$  of murine TNF- $\alpha$  for 18 h.  $1.7 \times 10^4$  and  $3.5 \times 10^4$  DiO-labeled MSCs (+/- MSV labeled with Alexa Fluor 555) in serum-free media were incubated for 24 h at 37 °C and 5%  $\text{CO}_2$  with MPVECs and MSCs in the top chamber with complete MSC media in the bottom chamber of the transwell. The top portion of the transwell was carefully washed with PBS to remove any nonadhered/migrated cells. The transwells were transferred to a well containing prewarmed TrypLE Express (Invitrogen) and incubated at 37 °C and 5%  $\text{CO}_2$  for 10 min. Transwells were removed and fixed in 4% PFA containing  $10 \times 10^{-6}$  M DRAQ5 for 30 min. Afterward, the membranes were extracted, placed on a glass slide, and mounted with Prolong Gold. While cells collected from the bottom of the transwell (i.e., transmigrated MSC) with TrypLE solution were spun down at 300  $\times g$  for 5 min, transferred to four chamber slides, and allowed to adhere at 37 °C and 5%  $\text{CO}_2$  for 2–3 h. Slides were fixed in 4% PFA, and mounted with Prolong Gold containing DAPI. Transwells were imaged using a Nikon A1 Confocal Imaging System housed in the HMRI Advanced Cellular and Tissue Microscopy Core Facility. Slides of transmigrated cells were imaged using Nikon Eclipse 80i fluorescence microscope equipped with a monochromatic Andor DL-604M camera by taking ten random FOV per slide and counting MSC using Nikon Elements software. Measurements represented samples from ten random FOV technical replicates per sample and concentration.

**Animal Care:** Animal studies were performed in accordance with the guidelines of the Animal Welfare Act and the Guide for the Care and Use of Laboratory Animals based on approved protocols by HMRI's Institutional Animal Care and Use Committee (Grant number: AUP-0618-0037). Female BALB/c (BALB/cAnNCrI; 4–6 week old) were purchased from Charles Rivers Laboratories and maintained as previously described.<sup>[32]</sup>

**IVM and Accumulation in Organs:** BALB/c mice were retro-orbitally administered with either free MSV (Alexa Fluor 555 conjugated) or MSV (Alexa Fluor 488 conjugated) within DiD-labeled MSC (at a ratio of 1:25). Organs (lungs, livers, spleens, and kidneys) were harvested and imaged using the IVM (confocal mode) by taking 20 random high-power images. In addition, at other predetermined times, the organs of mice were collected and imaged for MSV and MSC distribution using IVM, following the same procedure. Afterward, organs were split for quantitative analysis and frozen sectioning. The IVM was equipped with an upright Nikon ATR laser scanning confocal microscope equipped with a resonance scanner, motorized and heated stage, and Nikon long working distance 4 $\times$  and 20 $\times$  dry plan-apochromat objectives. Measurements represented a total of 39, 25, or 12 random FOV taken from three mice for liver, spleen, and kidney, respectively.

**Inflamed Ear Homing:** The right ears of mice were inflamed using *Escherichia coli* LPS (Sigma-Aldrich) as previously described.<sup>[62]</sup> Briefly, mice were anesthetized followed by an injection of 30  $\mu\text{g}$  of LPS (1 mg  $\text{mL}^{-1}$ ) in PBS being injected into the base of the right ear while 10–30  $\mu\text{L}$  of PBS was injected into the other. MSCs and M&Ms (25:1) were collected, stained with DiD, and passed through a 40  $\mu\text{m}$  cell strainer (BD).<sup>[63]</sup> For each mouse,  $1 \times 10^6$  MSCs were injected retro-orbitally 24 h post-LPS injection. Whole animal fluorescence and BLI for MSC and inflammation (respectively) was assessed using an IVIS Spectrum. For luminol, mice were imaged for BLI 5 min after i.p. administration of 5 mg (250–300 mg  $\text{kg}^{-1}$ ) of luminol (Sigma-Aldrich) for 5 min at medium binning and an f/stop of 1. Resulting images were analyzed with Living Image software. Measurements represented samples from at least four mice ( $n \geq 4$ ) for all times and both groups. For IVM imaging, mice were imaged at 24, 48, and 72 h. For delineation of vasculature, 40  $\mu\text{L}$  of FITC-dextran (70 kDa; Sigma-Aldrich) was injected retro-orbitally, just prior to imaging. Images were acquired by taking a z-stack of 50  $\mu\text{m}$  with a

step size of 5  $\mu\text{m}$  and analyzed for the number of MSCs present in each section using Nikon Elements. Measurements represented at least eight random FOV taken from three mice at all times and groups.

**Inflammatory Therapy—Local Inflammation:** The ears of mice were inflamed with an injection of 10  $\mu\text{L}$  of LPS and imaged for inflammation with BLI, as described above. BLI was measured before LPS, 3, 9, and 24 h after LPS administration. Mice ( $n = 5$ ) were separated into groups for: 1) untreated; 2) free IL10 (1 and 3  $\mu\text{g kg}^{-1}$ ); 3) IL10@MSV (1 and 6  $\mu\text{g kg}^{-1}$ ); 4) MSC ( $1 \times 10^6$  per mouse); 5) IL10@M&Ms ( $1 \times 10^6$  per mouse carrying 1  $\mu\text{g kg}^{-1}$  of IL10). 6 h after administration of LPS, mice were treated by injecting treatments retro-orbitally (IL10@MSV, MSC, and IL10@M&Ms), directly into ear (free IL10) or no treatment (untreated). Mice were followed with BLI until 24 h. Images were analyzed using the Living Image software, and the average radiance in both ears was calculated. Measurements represented samples from at least three mice ( $n \geq 3$ ) for all times and groups.

**Inflammatory Therapy—Systemic Inflammation:** The sepsis-related acute lung injury model was established in BALB/c mice by a lethal dose (i.p.) of LPS at 15  $\text{mg kg}^{-1}$ . Mice ( $n = 5$ ) were separated into groups for: 1) untreated; 2) free DEX (1  $\text{mg kg}^{-1}$ ,  $n = 4$ ; and 5  $\text{mg kg}^{-1}$ ); 3) DEX@MSV (1  $\text{mg kg}^{-1}$ ); 4) MSC ( $1 \times 10^6$  per mouse); 5) MSC ( $1 \times 10^6$  per mouse) plus free DEX (5  $\text{mg kg}^{-1}$ ); 6) DEX@M&Ms ( $1 \times 10^6$  per mouse carrying 1  $\text{mg kg}^{-1}$  of DEX). 30 min after LPS administration, mice were treated by injecting treatments retro-orbitally or no injection for untreated. Mice were monitored for survival for 120 h.

**Histology—Local Inflammation:** Explanted mice ears were cut by a biopsy pouch centered in the middle zone (diameter 8 mm), washed twice with PBS, embedded at the hedge in O.C.T. (Tissue-Tek O.C.T. Compound, Sakura Finetek), and instantly frozen in liquid nitrogen. 10  $\mu\text{m}$  thick slides were obtained by cutting ears block with a cryostat at  $-20^\circ\text{C}$ . For H&E staining, slides were thawed, hydrated, washed, and stained with hematoxylin and eosin (Sigma-Aldrich). H&E stained section was imaged using a 20 $\times$  objective on an EVOS FL Cell Imaging System microscope.

**Histology—Systemic Inflammation:** Harvested lungs were stored in 10% buffered formalin overnight, and then transferred to 70% ethanol. Tissues were then embedded in paraffin, and 5  $\mu\text{m}$  sections were placed on microscope slides by HMRI's Research Pathology Core. Sections were washed twice in fresh xylene for 10 min and rehydrated with decreasing ethanol concentrations (10 min for each step). Sections were stained with Masson's Trichrome (Abcam) for histological examination. Stained sections were then imaged using a 4 $\times$  or 20 $\times$  objective on a Nikon Eclipse 80i upright microscope equipped with a color Nikon DS-Fi1 camera and exported using the Nikon Elements software.

**Cytokine Analysis:** For sepsis-related acute lung injury model, plasma was collected at 18 and 120 h (only for DEX@M&Ms) and stored at  $-80^\circ\text{C}$ . Protein concentration was determined by Bradford assay (Bio-Rad) using albumin as reference for the standard curve. Plasma levels of TNF- $\alpha$  were measured using Quantikine ELISA kit (R&D Systems, Minneapolis, MN, USA) using the manufacturer's protocol. Samples were pooled ( $n = 4$ ), and samples were added to each well and incubated for 2 h at RT. Detection antibody was added and incubated for 2 h at RT, and then the substrate solution was added for 30 min. The reaction was stopped using an acid stop solution. Samples were measured for absorbance at 450 nm using a Synergy H4 BioTek plate reader. Measurements represented samples from at least three mice ( $n \geq 3$ ) with a technical triplicate.

**Statistical Analysis:** Statistics were calculated with GraphPad Prism 6 software. Statistics for IL10 release, firm adhesion, crawling, transmigration, and local inflammatory treatment analysis with BLI were analyzed with a two-way ANOVA with a Šidák post-hoc test (adhesion, transmigration, IL10 release), or a Tukey post-hoc test (crawling), or no correction (local inflammatory treatment) for multiple comparisons. No corrections were performed for local inflammatory treatment to reduce masking and the possibility of multiple comparisons in identifying a false negative. For docking and migration to inflammatory stimuli, statistics were analyzed using a one-way ANOVA with a Tukey post-hoc test to correct for multiple comparisons. Statistics for organ accumulation and fluorescence, BLI and

IVM imaging of MSC targeting, and plasma TNF- $\alpha$  analysis were analyzed using an unpaired, two-tailed  $t$  test. Survival data were analyzed using survival curve analysis with curve comparison using a Log-rank (Mantel-Cox) test. Outliers for crawling (both velocity and distance), IL10 release, imaging of MSC targeting (fluorescence, BLI, and IVM), local inflammatory treatment analysis with BLI, and cytokine analysis of plasma were identified using an Iterative Grubbs with an alpha of 0.001 (crawling) or Grubbs with an alpha of 0.2 (IL10 release, MSC targeting, local inflammatory treatment, and plasma cytokines). The allocation of the animals to the different groups of treatment was at random but were not performed blindly. Sample size estimation was approximated based on previous pilot studies or similar studies done in the past. In all cases: \* $p < 0.05$ ; \*\* $p < 0.01$ ; \*\*\* $p < 0.001$ ; \*\*\*\* $p < 0.0001$ ; and UD indicated that the value was undetected. Unless otherwise noted, all values were represented as mean  $\pm$  s.e.m.

## Supporting Information

Supporting Information is available from the Wiley Online Library or from the author.

## Acknowledgements

The authors would like to thank Dr. Mauro Ferrari of HMRI for helpful discussions on manuscript preparation and on the use of MSV. This work was financially supported by the NIH (5U54CA143837 and 1R21CA190024), the William Randolph Hearst Foundation, and the Cullen Trust for Health Care. In addition, J.O.M. was supported by the NIH predoctoral fellowships F31CA154119 and TL1RR024147. The authors would also like to thank Dr. Enrica De Rosa and HMRI Intravital Microscopy Core for IVM setup, acquisition, and analysis, Dr. David Haviland and HMRI Flow Cytometry Core Facility for flow cytometry setup and acquisition, Dr. Kemi Cui and HMRI Advanced Cellular and Tissue Microscope Core Facility for traditional confocal scanning services, HMRI Small Animal Imaging Core for access to IVIS Spectrum, HMRI Microscopy - SEM/AFM Core for access to Nova NanoSEM 230, HMRI Research Pathology Core for tissue preparation, Dr. Junping You for animal manipulation, Dr. Bruna Corradetti for mouse MSC isolation and characterization, Dr. Jana S. Burchfield and Megan Livingston for constructive edits of this manuscript, and Dr. Erika L. Spaeth, Vivek Kuran, Sebastian Powell, Nupur Basu, Chibuike Ofoegbuna, Katy R. Lipscomb, Anna Pastò, and Christian Boada for assistance with various experiments including MSC maintenance, preparation of therapeutic components, assistance with animal experiments, and histology.

## Conflict of Interest

The authors declare no conflict of interest.

## Keywords

drug delivery, inflammation, mesenchymal stromal/stem cells, nanovectors, sepsis

Received: April 3, 2020  
Revised: September 22, 2020  
Published online: October 13, 2020

[1] F. Taraballi, A. Pastò, G. Bauza, C. Varner, A. Amadori, E. Tasciotti, *J. Immunol. Regener. Med.* **2019**, *4*, 100017

- [2] A. I. Caplan, D. Correa, *Cell Stem Cell* **2011**, 9, 11.
- [3] M. A. Fischbach, J. A. Bluestone, W. A. Lim, *Sci. Transl. Med.* **2013**, 5, 179ps7.
- [4] M. B. Murphy, K. Moncivais, A. I. Caplan, *Exp. Mol. Med.* **2013**, 45, e54.
- [5] J. Ankrum, J. M. Karp, *Trends Mol. Med.* **2010**, 16, 203.
- [6] R. H. Lee, A. A. Pulin, M. J. Seo, D. J. Kota, J. Ylostalo, B. L. Larson, L. Semprun-Prieto, P. Delafontaine, D. J. Prockop, *Cell Stem Cell* **2009**, 5, 54.
- [7] W. R. Otto, N. A. Wright, *Fibrog. Tissue Repair* **2011**, 4, 20.
- [8] E. Blanco, H. Shen, M. Ferrari, *Nat. Biotechnol.* **2015**, 33, 941.
- [9] J. O. Martinez, B. S. Brown, N. Quattrocchi, M. Evangelopoulos, M. Ferrari, E. Tasciotti, *Chin. Sci. Bull.* **2012**, 57, 3961.
- [10] E. Tasciotti, X. Liu, R. Bhavane, K. Plant, A. D. Leonard, B. K. Price, M. M.-C. Cheng, P. Decuzzi, J. M. Tour, F. Robertson, M. Ferrari, *Nat. Nanotechnol.* **2008**, 3, 151.
- [11] J. Wolfram, H. Shen, M. Ferrari, *J. Controlled Release* **2015**, 219, 406.
- [12] J. O. Martinez, A. Parodi, X. Liu, M. G. Kolonin, M. Ferrari, E. Tasciotti, *Small* **2013**, 9, 1696.
- [13] J. O. Martinez, C. Chiappini, A. Ziemys, A. M. Faust, M. Kojic, X. Liu, M. Ferrari, E. Tasciotti, *Biomaterials* **2013**, 34, 8469.
- [14] J. O. Martinez, M. Evangelopoulos, R. Bhavane, S. Acciaro, F. Salvatore, X. Liu, M. Ferrari, E. Tasciotti, *Curr. Drug Targets* **2015**, 16, 1582.
- [15] S. Näkki, J. O. Martinez, M. Evangelopoulos, W. Xu, V.-P. Lehto, E. Tasciotti, *ACS Appl. Mater. Interfaces* **2017**, 9, 23441.
- [16] A. L. Van De Ven, P. Kim, O. Haley, J. R. Fakhoury, G. Adriani, J. Schmulen, P. Moloney, F. Hussain, M. Ferrari, X. Liu, S.-H. Yun, P. Decuzzi, *J. Controlled Release* **2012**, 158, 148.
- [17] M. P. Scavo, E. Gentile, J. Wolfram, J. Gu, M. Barone, M. Evangelopoulos, J. O. Martinez, X. Liu, C. Celia, E. Tasciotti, E. Vilar, H. Shen, *Colloids Surf., B* **2015**, 136, 694.
- [18] J. O. Martinez, M. Evangelopoulos, V. Karun, E. Shegog, J. A. Wang, C. Boada, X. Liu, M. Ferrari, E. Tasciotti, *Biomaterials* **2014**, 35, 9824.
- [19] A. Parodi, N. Quattrocchi, A. L. Van De Ven, C. Chiappini, M. Evangelopoulos, J. O. Martinez, B. S. Brown, S. Z. Khaled, I. K. Yazdi, M. V. Enzo, L. Isenhardt, M. Ferrari, E. Tasciotti, *Nat. Nanotechnol.* **2013**, 8, 61.
- [20] C. J. Tsao, L. Pandolfi, X. Wang, S. Minardi, C. Lupo, M. Evangelopoulos, T. Hendrickson, A. Shi, G. Storci, F. Taraballi, E. Tasciotti, *ACS Appl. Mater. Interfaces* **2018**, 10, 44344.
- [21] A. C. Anselmo, S. Mitragotri, *J. Controlled Release* **2014**, 190, 531.
- [22] W. Chen, L. Fu, X. Chen, *J. Controlled Release* **2015**, 219, 560.
- [23] N. L. Klyachko, R. Polak, M. J. Haney, Y. Zhao, R. J. Gomes Neto, M. C. Hill, A. V. Kabanov, R. E. Cohen, M. F. Rubner, E. V. Batrakova, *Biomaterials* **2017**, 140, 79.
- [24] R. Polak, R. M. Lim, M. M. Beppu, R. N. M. Pitombo, R. E. Cohen, M. F. Rubner, *Adv. Healthcare Mater.* **2015**, 4, 2832.
- [25] A. J. Swiston, C. Cheng, S. H. Um, D. J. Irvine, R. E. Cohen, M. F. Rubner, *Nano Lett.* **2008**, 8, 4446.
- [26] B. D. Chithrani, W. C. W. Chan, *Nano Lett.* **2007**, 7, 1542.
- [27] Y. Wang, Q. Wu, K. Sui, X.-X. Chen, J. Fang, X. Hu, M. Wu, Y. Liu, *Nanoscale* **2013**, 5, 4737.
- [28] A. Uccelli, L. Moretta, V. Pistoia, *Nat. Rev. Immunol.* **2008**, 8, 726.
- [29] S. Lee, S. Kivimäe, A. Dolor, F. C. Szoka, *J. Controlled Release* **2016**, 240, 527.
- [30] J. Zhang, X. Huang, H. Wang, X. Liu, T. Zhang, Y. Wang, D. Hu, *Stem Cell Res. Ther.* **2015**, 6, 234.
- [31] E. Tasciotti, B. Godin, J. O. Martinez, C. Chiappini, R. Bhavane, X. Liu, M. Ferrari, *Mol. Imaging* **2011**, 10, 56.
- [32] J. O. Martinez, C. Boada, I. K. Yazdi, M. Evangelopoulos, B. S. Brown, X. Liu, M. Ferrari, E. Tasciotti, *Small* **2013**, 9, 1722.
- [33] K. Asadullah, W. Sterry, H. D. Volk, *Pharmacol. Rev.* **2003**, 55, 241.
- [34] D. Sarkar, J. A. Ankrum, G. S. L. Teo, C. V. Carman, J. M. Karp, *Biomaterials* **2011**, 32, 3053.
- [35] G. S. L. Teo, J. A. Ankrum, R. Martinelli, S. E. Boetto, K. Simms, T. E. Sciuto, A. M. Dvorak, J. M. Karp, C. V. Carman, *Stem Cells* **2012**, 30, 2472.
- [36] K. Ley, C. Laudanna, M. I. Cybulsky, S. Nourshargh, *Nat. Rev. Immunol.* **2007**, 7, 678.
- [37] D. A. Jones, C. W. Smith, L. V. Mcintire, *Biomaterials* **1996**, 17, 337.
- [38] S. Gross, S. T. Gammon, B. L. Moss, D. Rauch, J. Harding, J. W. Heinecke, L. Ratner, D. Piwnica-Worms, *Nat. Med.* **2009**, 15, 455.
- [39] K. Guilloteau, I. Paris, N. Pedretti, K. Boniface, F. Juhaux, V. Huguier, G. Guillet, F.-X. Bernard, J.-C. Lecron, F. Morel, *J. Immunol.* **2010**, 184, 5263.
- [40] D. Rocksén, B. Lilliehook, R. Larsson, T. Johansson, A. Bucht, *Clin. Exp. Immunol.* **2000**, 122, 249.
- [41] S. Spence, M. K. Greene, F. Fay, E. Hams, S. P. Saunders, U. Hamid, M. Fitzgerald, J. Beck, B. K. Bains, P. Smyth, E. Themistou, D. M. Small, D. Schmid, C. M. O'kane, D. C. Fitzgerald, S. M. Abdelghany, J. A. Johnston, P. G. Fallon, J. F. Burrows, D. F. McAuley, A. Kissenpfennig, C. J. Scott, *Sci. Transl. Med.* **2015**, 7, 303ra140.
- [42] K. Németh, A. Leelahavanichkul, P. S. T. Yuen, B. Mayer, A. Parmelee, K. Doi, P. G. Robey, K. Leelahavanichkul, B. H. Koller, J. M. Brown, X. Hu, I. Jelinek, R. A. Star, É. Mezey, *Nat. Med.* **2009**, 15, 42.
- [43] A. Brooks, K. Futrega, X. Liang, X. Hu, X. Liu, D. H. G. Crawford, M. R. Doran, M. S. Roberts, H. Wang, *Stem Cells Transl. Med.* **2018**, 7, 78.
- [44] O. Levy, W. Zhao, L. J. Mortensen, S. Leblanc, K. Tsang, M. Fu, J. A. Phillips, V. Sagar, P. Anandakumaran, J. Ngai, C. H. Cui, P. Eimon, M. Angel, C. P. Lin, M. F. Yanik, J. M. Karp, *Blood* **2013**, 122, e23.
- [45] L. Pascucci, V. Coccè, A. Bonomi, D. Ami, P. Ceccarelli, E. Ciusani, L. Viganò, A. Locatelli, F. Sisto, S. M. Doglia, E. Parati, M. E. Bernardo, M. Muraca, G. Alessandri, G. Bondiolotti, A. Pessina, *J. Controlled Release* **2014**, 192, 262.
- [46] S. H. Ranganath, O. Levy, M. S. Inamdar, J. M. Karp, *Cell Stem Cell* **2012**, 10, 244.
- [47] J. S. Ananta, B. Godin, R. Sethi, L. Moriggi, X. Liu, R. E. Serda, R. Krishnamurthy, R. Muthupillai, R. D. Bolskar, L. Helm, M. Ferrari, L. J. Wilson, P. Decuzzi, *Nat. Nanotechnol.* **2010**, 5, 815.
- [48] R. Xu, G. Zhang, J. Mai, X. Deng, V. Segura-Ibarra, S. Wu, J. Shen, H. Liu, Z. Hu, L. Chen, Y. Huang, E. Koay, Y. Huang, J. Liu, J. E. Ensor, E. Blanco, X. Liu, M. Ferrari, H. Shen, *Nat. Biotechnol.* **2016**, 34, 414.
- [49] C. D. Buckley, D. W. Gilroy, C. N. Serhan, B. Stockinger, P. P. Tak, *Nat. Rev. Immunol.* **2013**, 13, 59.
- [50] S. Zhang, J. Ermann, M. D. Succi, A. Zhou, M. J. Hamilton, B. Cao, J. R. Korzenik, J. N. Glickman, P. K. Vemula, L. H. Glimcher, G. Traverso, R. Langer, J. M. Karp, *Sci. Transl. Med.* **2015**, 7, 300ra128.
- [51] D. W. Gilroy, T. Lawrence, M. Perretti, A. G. Rossi, *Nat. Rev. Drug Discovery* **2004**, 3, 401.
- [52] Z. Cheng, A. Al Zaki, J. Z. Hui, V. R. Muzykantov, A. Tsourkas, *Science* **2012**, 338, 903.
- [53] K. Park, *ACS Nano* **2013**, 7, 7442.
- [54] M. Ferrari, *Nat. Rev. Cancer* **2005**, 5, 161.
- [55] J. A. Ankrum, J. F. Ong, J. M. Karp, *Nat. Biotechnol.* **2014**, 32, 252.
- [56] S. Geiger, D. Hirsch, F. G. Hermann, *Eur. Respir. Rev.* **2017**, 26, 170044.
- [57] R. Molinaro, C. Corbo, J. O. Martinez, F. Taraballi, M. Evangelopoulos, S. Minardi, I. K. Yazdi, P. Zhao, E. De Rosa, M. B. Sherman, A. De Vita, N. E. Toledano Furman, X. Wang, A. Parodi, E. Tasciotti, *Nat. Mater.* **2016**, 15, 1037.

- [58] B. Corradetti, F. Taraballi, S. Powell, D. Sung, S. Minardi, M. Ferrari, B. K. Weiner, E. Tasciotti, *Stem Cells Dev.* **2015**, *24*, 1112.
- [59] M. Soleimani, S. Nadri, *Nat. Protoc.* **2009**, *4*, 102.
- [60] C. Chiappini, E. Tasciotti, J. R. Fakhoury, D. Fine, L. Pullan, Y.-C. Wang, L. Fu, X. Liu, M. Ferrari, *ChemPhysChem* **2010**, *11*, 1029.
- [61] S. Minardi, L. Pandolfi, F. Taraballi, E. De Rosa, I. K. Yazdi, X. Liu, M. Ferrari, E. Tasciotti, *ACS Appl. Mater. Interfaces* **2015**, *7*, 16364.
- [62] C. Xu, D. Miranda-Nieves, J. A. Ankrum, M. E. Matthiesen, J. A. Phillips, I. Roes, G. R. Wojtkiewicz, V. Juneja, J. R. Kultima, W. Zhao, P. K. Vemula, C. P. Lin, M. Nahrendorf, J. M. Karp, *Nano Lett.* **2012**, *12*, 4131.
- [63] B. Corradetti, F. Taraballi, J. O. Martinez, S. Minardi, N. Basu, G. Bauza, M. Evangelopoulos, S. Powell, C. Corbo, E. Tasciotti, *Sci. Rep.* **2017**, *7*, 7991.